Geometrical preference of anchoring sites in the unicellular organism *Stentor coeruleus*

Syun Echigoya[1,2]*, Takuya Ohmura[1,3], Katsuhiko Sato[4], Toshiyuki Nakagaki[1,3], Yukinori Nishigami[1,3]*

[1] Research Center of Mathematics for Social Creativity, Research Institute for Electronic Science, Hokkaido University, N20W10, Kita-ku, Sapporo, 001-0020, Japan.
[2] Institute for Integrated Innovations, Hokkaido University, N21W10, Kita-ku, Sapporo, 001-0021, Japan.
[3] Graduate School of Life Science, Hokkaido University, N10W8, Kita-ku, Sapporo, 060-0810, Japan.
[4] Program of Mathematics and Informatics, Faculty of Science, Academic Assembly, University of Toyama, 3190 Gofuku, Toyama 930-8555, Japan.
*Correspondence: syun@es.hokudai.ac.jp (SE); nishigami@es.hokudai.ac.jp (YN)

Abstract

Organisms often inhabit environments comprising complex structures across various scales. Animals rely on visual information from surrounding geometrical structures for navigation. Even at the microscale, various microsediments form complex structures in microbial habitats. The movement of microorganisms is passively affected by collisions and hydrodynamic interactions with surrounding structures. However, the influence of microenvironmental geometry on behavioral changes of unicellular organisms that lack visual perception remains unclear. Here, we developed geometrically structured chambers to investigate anchoring site preferences in the swimming ciliate *Stentor coeruleus*. *S. coeruleus* tended to anchor in narrow areas based on geometrical features such as corner angle, depth, and curvature at the corner end. Before anchoring, free-swimming *S. coeruleus* changed its behavior to move along the boundary wall of the chambers, accompanied by Ca^{2+}-induced asymmetrical body deformation. To further investigate how *S. coeruleus* moves along the wall continuously, we conducted a hydrodynamic simulation and revealed that the asymmetric morphology causes asymmetric propulsive forces, explaining wall-following behavior through physical interactions with a wall. Thus, morphological change near a wall causes wall-following behavior, facilitating the identification of these narrow anchoring sites. Our findings indicate that environmental geometry drives behavioral transitions in *S. coeruleus* through simple biophysical processes, enabling spatial selection without visual cues. Overall, these results suggest that microgeometry plays a key role in shaping ecological niches for unicellular microorganisms.

Significance statement

Animals use various natural structures as landmarks for navigation. In microorganism habitats, microsediments also form geometrically complex environments. Is there a relationship between the geometrical features of structures and the behavior in unicellular organisms lacking visual cues? Here we report that the free-swimming unicellular organism, *Stentor coeruleus*, selects the anchoring sites depending on the surrounding shapes. Further observations and numerical simulations reveal that an asymmetric morphological change causes a temporary switch from ballistic to wall-following exploration, driven by surrounding structures. These results indicate that one simple behavioral response underlies the preference of anchoring sites with specific geometrical features in non-neural unicellular organisms. The findings shed light on the role of microenvironmental geometry in forming ecological niches for microorganisms.

Introduction

Navigation is a fundamental survival strategy for heterogeneous environments. Animals, such as insects and mammals, use global information from the sun, light polarization, magnetic fields, and gravity for navigation (1–5). Moreover, ants, bees, and mantis shrimp use various natural structures in their habitats as panoramic views or landmarks for navigation (6–9). In a recent study, environmental geometry obtained through visual input was encoded by a single cell in the dorsal subiculum in mice (10). Thus, various behavioral experiments and electrophysiological analyses have suggested that ubiquitous obstacles and their geometrical shapes play important roles in animal navigation (11).

Spatial exploration in unicellular organisms has been studied based on the taxis of primitive navigation systems that react to light, magnetic fields, electric fields, gravity, and chemical substances (12–14). Spatiotemporal changes in external stimulus cause Ca^{2+} influx into cilia through channels (15, 16). These bioelectrical signals modulate ciliary beating patterns and motility (17–21), leading to tactic behaviors (22). Active regulation of ciliary beating in algae and shape changes in ciliates exhibit adaptive responses originating from interactions with hydrodynamic constraints (23, 24).

In microorganism habitats, many microsediments form geometrically complex environments. In the last decade, the physical effect of geometrical structures on the behavior of microorganisms has been investigated through mechanical collision or hydrodynamic interaction (25–34). However, the relationship between the intrinsic behavioral changes of microorganisms and the surrounding geometrical features is not yet understood.

In this study, we focused on the anchoring behavior of the swimming ciliate *Stentor coeruleus*, which transitions between free-swimming and anchoring to a substrate in aquatic environments (Fig. 1A). *S. coeruleus* has been studied for its phototaxis and chemotaxis (35, 36) and learning systems such as habituation (37–39), hierarchical response (40–42) and cooperative feeding behavior (43), drawing increasing attention to its cognitive systems. *S. coeruleus* has (i) hair-like organelles (membranella bands [MBs]), which produce a propulsive force for swimming and feeding, around its anterior and (ii) an anchoring organ (holdfast) at its posterior end (35, 44). Under culture conditions, we often found *S. coeruleus* anchoring to rice or oat grains added to promote bacterial growth as a nutrient source (Fig. 1B, C). Under laboratory conditions, *S. coeruleus* also anchored in narrow sites in natural sediments, such as the exuvia of an aquatic insect (Fig. 1D). When sampling from a pond, anchoring *S. coeruleus* were often found on a geometrically complex sediment (Fig. 1E). *S. coeruleus* tended to anchor within narrow areas and not across the entire surface of the sediments (Fig. 1B–E). The environmental complexity in both culture and natural conditions made it difficult to identify the factors influencing the selection of anchoring sites.

Herein, we developed three types of geometrically structured chambers using a sub-millimeter-scale fabrication technique to investigate the anchoring behavior of *S. coeruleus*, extending our previous study (32). *S. coeruleus* exhibited a geometrical preference of anchoring sites based on the corner angle, depth, and curvature at the corner ends formed by a structure and chamber walls. This geometrical preference exhibited a correlation with body length in the swimming state. Before anchoring in the geometrical structural chambers, *S. coeruleus* displayed a behavioral change from exploratory to wall-following behavior, which was physically explained by asymmetric propulsion accompanying cell deformation regulated by intracellular Ca^{2+}. This study addresses how environmental geometry influences exploratory and anchoring behavior, shedding light on how complex environments guide site selection of unicellular organisms in narrow areas.

Results

Geometrical preferences of anchoring sites in geometrically complex environments

We developed quasi-2D geometrically structured chambers to investigate the geometrical features of the anchoring sites of *S. coeruleus*. We observed the behavior of a single *S. coeruleus* for approximately 40 min under dim red light to prevent phototactic responses in these chambers (Fig. 2A). *S. coeruleus* freely swam with a spiral trajectory exploring the chambers. The swimming speed temporarily decreased around the walls and corners owing to collisions caused by the geometrical complexity of the chambers (Fig. 2B). To analyze the overview of the behaviors of *S. coeruleus*, we quantified the swimming speed and cell length. Most cells exhibited a length of 0.4 mm and swam steadily at a speed of 0.5–1.0 mm/s. Subsequently, the swimming cells switched to the anchoring state accompanied by elongation and deceleration (Fig. 2C and Movie S1). Some cells repeatedly switched their states between swimming and anchoring, leading to behavioral complexity. We measured the locations of the cells and the number of anchoring events, focusing on the three geometrical features: corner angle, depth, and curvature.

First, in a symmetrical right-triangle chamber, *S. coeruleus* anchored more frequently at 45° corners than at a 90° corner, and the number of anchoring events in each 45° corner was not significantly different (Fig. 2D, I, binomial test, $p = 0.36$). In an asymmetrical right-triangle chamber, *S. coeruleus* anchored to a corner with a small angle (Fig. 2D). Next, we designed an environment containing corner angles ranging from 30° to 150° by introducing protruding rod-like structures along the outer edge of the chambers. Subsequently, the cells showed a tendency to anchor at corners with small angles (Fig. 2E). Although 27% of anchoring events (6/22) were observed outside the corners, the number of anchoring events per area was relatively low compared with that at corners with acute angles (Fig. 2J). Thus, corners with angles less than 45° showed a significant increase in both the number of anchoring events and total anchoring duration (Fig. 2J and Supplementary material, Fig. S2).

Second, we developed a geometrically structured chamber featuring four types of corners, each having a depth and protruding rod-like structures with different lengths at a fixed angle. In the chamber, *S. coeruleus* tended to anchor to corners with a high depth (Fig. 2F and Supplementary material, Fig. S2). Although the number of anchoring events and total anchoring duration exhibited a positive correlation with the corner depth, several cells anchored at the corner formed by the short protrusion (depth: ~0.4 mm) (Fig. 2K). The anchoring frequency, which was calculated as the number of anchoring events per specific surface area, was higher at this corner than at other corners (Fig. 2K). In channels with different lengths, *S. coeruleus* anchored at channels deeper than 0.4 mm (Fig. 2G, L). However, the cells did not frequently anchor to the channels with a depth more than twice their cell length; the highest anchoring frequency was observed at a depth of 0.45 mm (Fig. 2L). Notably, while the cells spent 75% of their total swimming time outside the channels, 85% of the anchoring events (33/39) were observed inside one of the channels (Supplementary material, Fig. S2).

Third, we arranged three types of corners with different two-dimensional curvatures in a star-shaped periodic layout at three locations. Fig. 2H represents the superimposed anchoring sites and durations at each corner type, showing a tendency to anchor near corners with a smaller curvature radius (<0.1 mm), which corresponds to the width of *S. coeruleus* (Fig. 2M). In addition, we investigated whether a hierarchy of geometrical features influenced the selection of anchoring sites by observing the anchoring behavior of these cells at corners with different angles and curvatures (Supplementary material, Fig. S2). Most cells anchored at sharper corners with a smaller angle. However, the secondary preferences in the selection of anchoring sites were unclear, suggesting no hierarchical prioritization of the anchoring sites.

Collectively, the aforementioned findings demonstrate that *S. coeruleus* selects anchoring sites based on the surrounding geometrical features and that the geometrical preferences scale with its cell size in the swimming state.

Behavioral process of anchoring in geometrically complex environments

To understand the anchoring behavior in the geometrically structured chambers, we focused on the behavioral transition from steady swimming to the trumpet-shaped anchored state and compared this transition between a simple circular chamber and geometrically structured chambers. We found two types of anchoring processes depending on the structural complexity of the environment (Fig. 3A). In the simple circular chamber, the cell monotonically elongated from a conical swimming shape to a trumpet shape during anchoring, consistent with previous reports (32, 45). In comparison, in the geometrically structured chambers, swimming *S. coeruleus* exhibited a transient contraction over a few seconds before elongation. This contraction in the geometrically structured chambers reduced the cell length to approximately 70% of the original, representing a significant decrease compared with the cell length in the simple circular chamber 30 s after each transition (Fig. 3B). The characteristic time of the transition from contraction to elongation was not observed owing to variability in the transition time among individual cells. Even in the geometrically structured chambers, some cells monotonically elongated in the anchoring transitions (Fig. 3A, B). The cellular length in the final state, measured as the maximum value in each transition, showed no significant difference in the anchoring processes across the three conditions (Fig. 3B).

To further understand the anchoring transition with temporal contraction, we examined the differences in swimming trajectories between the steady swimming state and the post-transition state within a behavioral window of up to 1 minute. In the steady swimming state, the cells explored the whole geometrically structured chambers, with the chamber wall affecting the swimming directions (Movie S2). After transitioning, cells adopted wall-following swimming behaviors, moving along even rod-like structures (Fig. 3C, Supplementary material, Fig. S4, and Movie S3). Compared with steady swimming cells, post-transition cells moved closer to the chamber wall, as indicated by the average distance between the cell center and the wall in two geometrically structured chambers (Fig. 3D). Furthermore, the ratio of wall-contact time to total time during the behavioral window following the transition was also significantly high (Fig. 3E). Thus, during the anchoring process in the geometrically structured chambers, *S. coeruleus* exhibits a wall-fallowing behavior following transient contraction, which precedes cell elongation.

Effect of intracellular Ca^{2+} concentration on the anchoring process accompanying cell shape changes

In the class Heterotrichea, including *Stentor*, cell deformation is regulated by intracellular Ca^{2+} concentration (46, 47). Therefore, to understand the biological mechanism of cell deformation during the anchoring process, we focused on the relationship between intracellular Ca^{2+} and cell deformation during the anchoring transition. Herein, we established the detergent-treated *S. coeruleus* model (Materials and Methods and Supplementary material, Fig. S5), modified from a previously established *Blepharisma* model (48). First, *S. coeruleus* were treated with Triton X-100 in a Ca^{2+}-free solution without extracellular adenosine triphosphate (ATP) to permeabilize the membrane (Fig. 4A). The cell models were 0.22 ± 0.05 mm long (mean ± SD; $n = 51$) and cone-shaped, which is usually seen in the swimming state (Fig. 4B). After demembranization above 4×10^{-8} M, the cell models adopted a droplet shape and their lengths decreased compared with those after demembranization in a Ca^{2+}-free condition (Fig. 4B).

The MBs and body cilia of the detergent-treated cell models exhibited beating after adding ATP at a final concentration of 4 mM in a Ca^{2+}-free condition (Fig. 4C). Although some *S. coeruleus* models showed posterior elongation forming a trumpet shape, this elongation was less frequent in models with an original length of <0.25 mm (Supplementary material, Fig. S5). Thus, we excluded the droplet-shaped cell models from further analysis of Ca^{2+}-dependent model elongation. Although the initial model lengths L_0 did not exhibit a significant difference at Ca^{2+} concentrations of $<10^{-6}$ M (Fig. 4D), the elongation was suppressed at Ca^{2+} concentrations of $>10^{-7}$ M (Fig. 4E). In low Ca^{2+} concentrations, the deformation ratios 1 min after ATP addition were 1.36 ± 0.11 in the Ca^{2+}-free condition and 1.38 ± 0.21 at $[Ca^{2+}] = 4 \times 10^{-8}$ M. Therefore, high Ca^{2+} concentration during detergent treatment induced contraction in *S. coeruleus* models in the absence of ATP. However, model elongation required ATP and occurred at low Ca^{2+} concentration.

Asymmetrical cell shape during transition hydrodynamically facilitates the wall-following behavior

Next, we examined how *S. coeruleus* achieved the wall-following behavior before anchoring without visual cues. *S. coeruleus* moves using cilia distributed along the entire cell surface (body cilia) and MBs located around the frontal field (oral plane) at the anterior end. The water current around the MBs is approximately 100 times stronger than that around the cell surface (body cilia) (44). We compared the orientation of the oral plane between the steady swimming and transition states (Fig. 3F). While the oral plane in the steady swimming state was symmetrical (θ_{oral} = 0.5° ± 4.6°; mean ± SD; n = 11 cells), the oral plane in the transition state was significantly tilted toward the ventral side (Fig. 3G, 30.5° ± 10.2°; mean ± SD; n = 11 cells). Oral angles were calculated from the orientation of the oral plane relative to the anterior–posterior axis. When the wall was absent on the ventral side, the cells swam in a circular trajectory, with the ventral side directed to the circular center owing to the torque induced by the asymmetric propulsion.

Based on cell deformation, we conducted a hydrodynamical simulation to investigate the mechanical relationship between the wall-following behavior and dorsoventral asymmetry of the oral plane. To construct the numerical *Stentor*, we defined point forces that were distributed only around the base of a conical object (Fig. 5A and Supplementary material, Fig. S6). The model excluded both body cilia activity and the effect of rotation around the long axis.

The elongated portion of the swimmer was horizontally displaced parallel to the base of the conical object, which constrains the swimmer's volume (Fig. 5B). While the symmetrical numerical *Stentor* approached the wall and then deflected away owing to the upward torque generated by hydrodynamic interactions (Fig. 5C), the numerical *Stentor* with asymmetrical propulsion turned toward the wall owing to self-generated downward torque and moved along the wall (Fig. 5D and Movie S4). When the downward torque caused by the asymmetrical distribution of propulsive forces exceeds the upward torque generated hydrodynamically, the net torque becomes zero, resulting from a direct repulsive force from the substrate, enabling the swimmer to move along the wall. With small asymmetricity (θ_{oral} = 5°–15°), the swimmer temporarily swam away from the wall owing to the near-wall hydrodynamic interactions and returned to the wall using self-generated downward torque, resulting in two motions repeatedly and causing wave-like trajectories (Fig. 5E). The oral angles in the wave-like trajectories of the simulation were rare in the experimental transition state (Fig. 3G). Therefore, the dorsoventral asymmetry of the propulsion physically explains the wall-following behavior of *S. coeruleus*.

Discussion

We quantified the detailed geometrical characteristics of narrow areas influencing the anchoring. The anchoring processes from swimming to adhering involved wall-following exploration with asymmetrical morphological change associated with intracellular Ca^{2+} concentrations. A mechanical model and observation of the cell deformation indicated that asymmetric propulsion facilitates the wall-following behavior not through continuous visual recognition, enabling final anchoring to narrow sites (Fig. 6).

The wall-following behavior was observed only in geometrically complex environments, indicating that an increase in contact with a wall due to the geometrical complexity induces the anchoring transition. Ciliates referred to as "swimming neuron" (49, 50) typically exhibit transient backward swimming upon collision against a wall, a response triggered by the bioelectric activity of the membrane potential through Ca^{2+} influx (33, 51–53). Consistent with this, our contracted permeabilized *Stentor* model with high Ca^{2+} concentration exhibited contraction, supporting an idea that increased contact triggers contraction. Owing to the asymmetric distribution of the contractile fiber myoneme (54), the contraction may tilt the oral plane, contributing to the asymmetric morphological change. Furthermore, the spatial positive correlation between backward swimming and anchoring (Fig. 2D, E, H and Supplementary material, Fig S3) suggests that increased contact stimulus induces *S. coeruleus* to transition to the wall-following behavior in a narrow area. The anchoring decision could depend on the physical constraints influenced by the geometrical features, which decreased around specific corners owing to physical constraints.

Although wall-following behavior is conserved across several organisms from unicellular species to animals (55), the wall-following behavior observed in *S. coeruleus* is not only novel but also characterized by two unique biophysical mechanisms. First, while hydrodynamic interactions of microswimmers with the wall have been widely investigated (56–58), our findings reveal a novel and simple hydrodynamic mechanism: asymmetric propulsive forces drive the thigmotactic behavior in this microswimmer. Second, although myoneme-induced rapid contractions in ciliates typically occur in milliseconds (59), the contraction duration observed in our study (Fig. 3A) was approximately 1000 times longer than that of a rapid contraction. The contraction during the anchoring process in *Stentor* has not been reported. Hence, our results indicate that the environmental complexity of our experimental chambers enables the observation of a novel behavioral transition.

Anchoring in narrower sites of geometrically structured chambers may help avoid predators, light exposure, and desiccation. Large predators rarely enter into narrow areas, which are covered by structures reducing light. Furthermore, under drying conditions, water is likely to accumulate in narrow areas owing to surface tension. Our results revealed rapid contraction in *Stentor*, likely to avoid predators, allowing the entire cell body to fit within the structural narrowness. Moreover, *Stentor* preys on swimming algae, *Chlamydomonas*, which aggregates at corners due to physical mechanisms (31). *Stentor* might be able to obtain the food despite being in stagnant narrow areas. Therefore, the adaptive behavioral transition of *S. coeruleus* observed in geometrically complex environments can be mechanically explained by the simple asymmetrical deformation of the cell.

In conclusion, we identified the geometrical features of the preferential anchoring sites of *S. coeruleus* using geometrically structured chambers. The anchoring process involves an active behavioral transition from steady swimming to wall-following exploration, driven by an increase in intracellular Ca^{2+} concentration, contributing to anchoring in narrow sites, which was only observed in geometrical structural chambers containing narrow areas. A simple mechanism of the asymmetric cell contraction physically explains the wall-following behavior. *S. coeruleus* anchors due to a decrease in motility

caused by the surrounding geometrical features. Subsequently, Ca^{2+} efflux induces elongation to a trumpet shape. Our findings provide evidence that even in the absence of a visual input, a unicellular organism ubiquitously utilizes microgeometrical features in its habitats. Diverse geometrical shapes in microhabitats create ecological niches for protists (60, 61), including *Stentor*, which play crucial roles in ecology, such as material circulation (62). These findings offer insights into primitive navigation systems in unicellular organisms and highlight the relationship between environmental geometry and ecological networks.

Materials and Methods

Cell culture

S. coeruleus were collected from the Shiribetsu River (42.81°N, 140.69°W) in Japan. The cultures were maintained using modified Peters' solution (63) containing an oat grain. Details are provided in the Supplementary material.

Observation of the anchoring behavior in geometrically structured chambers

Geometrical observation chambers were fabricated via a molding process. These molds were designed using the three-dimensional (3D) CAD software Fusion360 (Autodesk, California, United States) (Supplementary material, Fig. S1). A milling machine, CAMM-3 Model PNC-3200 (Roland DG Corporation, Hamamatsu, Japan), equipped with a microend mill was used to fabricate molds by cutting the modeling wax ZW-100 (Roland DG Corporation, Hamamatsu, Japan). Prior to making the geometrically structured chambers, 2.0% (w/v) agarose solution was prepared from the modified Peters' solution and PrimeGel (Agarose LE 1–20K, Takara Bio, Shiga, Japan). After the mixture was melted, it was poured into the mold and sealed with a glass slide to flatten the upper surface (Supplementary material, Fig. S1). After solidification, the gel chamber was detached from the mold.

Prior to observation, cells were transferred into fresh culture medium twice to prevent chemical effects, allowing the cells to acclimate for several hours. The geometrically structured chambers were rinsed with fresh medium on a glass slide, and the chamber was filled with the medium and sealed with a coverslip pretreated with oxygen plasma for 10–20 s to increase surface hydrophilicity (PC-400T, STREX, Osaka, Japan). An individual swimming *S. coeruleus* was gently released into the gap between the chamber and the above coverslip. Subsequently, the observation chamber was entirely sealed by sliding the coverslip into place. The behaviors were recorded using a CMOS camera, ORCA-spark C11440-36U (Hamamatsu Photonics, Hamamatsu, Japan) mounted on a stereo microscope, SZX16 (Evident, Tokyo, Japan). The images were acquired at 4 frames per second (fps) with a 50 ms exposure time. Imaging was conducted under red-filtered brightfield illumination and minimal light intensity to prevent phototactic responses in *S. coeruleus*.

Quantification of geometrical preferences of anchoring sites

Anchoring sites and durations were manually obtained, and anchoring events shorter than 10 s were excluded. Anchoring site preferences in the Results section were quantified using two metrics: 1) total number of anchoring events in each defined region, which included a characteristic geometrical feature formed by an outer wall of the geometrically structured chamber and 2) anchoring frequency, defined as the number of anchoring events divided by area of each region. Detailed definitions of each region are provided in the Supplementary material.

To evaluate the effect of corner angle on anchoring in right triangle chambers, an asymmetry index was calculated from the number of anchoring events in large θ_{large} or small θ_{small} angles per area, as defined below.

$$\text{Asymmetry index } (\alpha) = (f^{\alpha}_{small} - f^{\alpha}_{large}) / (f^{\alpha}_{small} + f^{\alpha}_{large}),$$

where α is a shape parameter in triangle chambers defined as $\theta_{large}/\theta_{small}$. The anchoring frequency in the α-shaped chamber, f^{α}_{i} is defined as

$$f^{\alpha}_{i} = (\text{number of the anchoring events})_i / \text{area}_i.$$

The geometrical values reported in the Results section were measured from the actual agarose chambers, rather than from the design.

Image analysis and quantification of behaviors in the geometrically structured chambers

Cell center and body length were extracted from image contours using ImageJ/Fiji (64) and Python 3.11.7 (https://www.python.org/). The recorded images were subtracted using a background image acquired from sequential frames. Gaussian blur was applied to the background-subtracted sequential images to reduce noise. Then, the images were binarized by applying the brightness thresholds. Cell length was calculated from the binary images as the sum of two distances measured from the center of the cell to its anterior and posterior ends (32). Since Gaussian blur caused overestimation of the body length by 20–100 μm, we corrected the measured lengths by comparing the cell outline and raw data. Swimming velocity was calculated from the displacement of the center of the cell. Both velocity and cell length data were smoothed by the median values of ± 10 s.

Comparison of anchoring transition with and without geometrical structures

To compare anchoring behaviors in the presence or absence of geometrical structures, we recorded individual behavior in a simple circular chamber using a CMOS camera, ORCA-Flash4.0 v2 (Hamamatsu Photonics, Hamamatsu, Japan), under red-filtered brightfield illumination with an exposure time of 50 ms at 4 fps with minimal light intensity. A simple circular chamber was fabricated using agarose gel into a quasi-two-dimensional disk of 0.3 mm thickness and 5 mm diameter.

We defined the start of the anchoring transition as the point when the cell deformed from its steady cone-shaped swimming form, and the end as the point when the cell became sufficiently elongated, indicating the final state. The cell length over time was normalized to the individual mean cell length in the steady-swimming state. We classified the behavioral transition as "contraction" when the mean length 30 s after deformation was shorter than that in the steady swimming state, and as "elongation" when it was longer.

To compare swimming trajectories during steady swimming and the transition before anchoring, we manually selected a helical steady-swimming phase and the transition section (each up to 1 min). The transition section was defined to start 15 s after cell deformation, excluding any period when the cell was anchored. The distance between the cell and the chamber wall was measured as the minimum distance between the cell center and the outer wall. Additionally, we quantified the dwell time of the cell within 0.15 mm of the outer wall to evaluate contact duration with the wall.

In these analyses, we calculated the mean values for each cell over its recording period and then calculated the mean and standard deviation (SD) for each population.

Measurement of the orientation angle of the oral plane

We selected one representative image to quantify the cellular shape in the steady swimming state and the wall-following state, with two body axes, anterior–posterior (AP) and dorsoventral (DV) (65), aligned to an image plane because the swimming *S. coeruleus* rotated along the AP axis. An oral plane is formed by a closed area of the MBs located at the periphery of the oral groove at the anterior end, causing a strong flow for swimming and feeding. We manually traced the oral plane from the images as a line and then measured the orientation angle between the AP axis and the normal vector of the oral plane, defining the positive direction as the ventral side. The AP axis was obtained from the long axis extracted by ellipsoidal fitting to the contour of the cell.

Development of a detergent-treated model of *S. coeruleus* and observation methods

We developed a detergent-treated *S. coeruleus* model modifying a cell model in *Blepharisma*, which is closely related to *Stentor*, as described in Matsuoka et al. 1991 (48). The detailed protocol, solution composition and observation conditions are provided in the Supplementary material.

Measurement of model length and evaluation of elongation

We manually segmented three points from the anterior to the posterior end and determined the model length as the total length of the two segmented lines (Supplementary material, Fig. S5). The elongation ratio was calculated by the initial length L_0, measured within 30 s after ATP addition, and the length L, measured 1 min after ATP addition. If accurate measurement of the length at the 1-min time point was not possible due to three-dimensional motion, the nearest available time frame was used.

Construction of a hydrodynamical model of a numerical *Stentor*

To investigate the movement of the numerical swimmer near the wall, we developed a conical swimmer model mimicking *Stentor*'s shape by deforming a spherical object with radius 1. Point forces mimicking ciliary beating were distributed around the base of the conical swimmer. The deformation method, propulsive force distribution and initial conditions for numerical simulations are described in the Supplementary material.

Computational simulation of movement in the numerical swimmer near a plane boundary

We computed the motion of the numerical swimmer in satisfying under fundamental constraints resulting from the nature of the viscous fluid (a computational algorithm was the same in Ohmura et al (26)). Detailed numerical methods were provided in Supplementary material.

Quantification and statistical analysis

Statistical analyses were conducted using scipy.stats version 1.11.4 in Python 3.11.7. Depending on the comparison, paired *t*-tests, Welch's *t*-tests, and one-way ANOVA were used. Test statistics and sample sizes are provided in the Figure legends and main text. Statistical significance was indicated as follows: n.s. (not significant, $p > 0.05$); $^{**}p < 0.01$; $^{***}p < 0.001$; $^{****}p < 0.0001$.

References

1. K. von Frisch, Die Polarisation des Himmelslichtes als orientierender Faktor bei den Tänzen der Bienen. *Experientia* **5**, 142–148 (1949).
2. R. Wehner, Neurobiology of polarization vision. *Trends Neurosci.* **12**, 353–359 (1989).
3. W. Wiltschko, R. Wiltschko, Magnetic compass of European robins. *Science* **176**, 62–64 (1972).
4. C. Walcott, R. P. Green, Orientation of homing pigeons altered by a change in the direction of an applied magnetic field. *Science* **184**, 180–182 (1974).
5. R. Wiltschko, W. Wiltschko, The discovery of the use of magnetic navigational information. *J. Comp. Physiol. A* **208**, 9–18 (2022).
6. A. Wystrach, G. Beugnon, Ants learn geometry and features. *Curr. Biol.* **19**, 61–66 (2009).
7. A. Wystrach, G. Beugnon, K. Cheng, Landmarks or panoramas: what do navigating ants attend to for guidance? *Front. Zool.* **8**, 21 (2011).
8. T. Collett, Insect navigation en route to the goal: multiple strategies for the use of landmarks. *J. Exp. Biol.* **199**, 227–235 (1996).
9. R. N. Patel, T. W. Cronin, Landmark navigation in a mantis shrimp. *Proc. R. Soc. B* **287**, 20201898 (2020).
10. Y. Sun, D. A. Nitz, X. Xu, L. M. Giocomo, Subicular neurons encode concave and convex geometries. *Nature* **627**, 821–829 (2024).
11. E. Chan, O. Baumann, M. A. Bellgrove, J. B. Mattingley, From objects to landmarks: the function of visual location information in spatial navigation. *Front. Psychol.* **3**, 304 (2012).
12. H. S. Jennings, *Behavior of the Lower Organisms* (Columbia University Press, 1906).
13. R. Blakemore, Magnetotactic bacteria. *Science* **190**, 377–379 (1975).
14. K. Y. Wan, G. Jékely, Origins of eukaryotic excitability. *Phil. Trans. R. Soc. B* **376**, 20190758 (2021).
15. K. Dunlap, Localization of calcium channels in *Paramecium caudatum*. *J. Physiol.* **271**, 119–133 (1977).
16. H. Machemer, A. Ogura, Ionic conductances of membranes in ciliated and deciliated *Paramecium*. *J. Physiol.* **296**, 49–60 (1979).
17. Y. Naitoh, R. Eckert, Ciliary orientation: controlled by cell membrane or by intracellular fibrils? *Science* **166**, 1633–1635 (1969).
18. Y. Naitoh, H. Kaneko, Reactivated triton-extracted models of *Paramecium*: modification of ciliary movement by calcium ions. *Science* **176**, 523–524 (1972).
19. H. Machemer, Cellular behaviour modulated by ions: Electrophysiological implications. *J. Protozool.* **36**, 463–487 (1989).
20. K. Shiba, S. A. Baba, T. Inoue, M. Yoshida, Ca^{2+} bursts occur around a local minimal concentration of attractant and trigger sperm chemotactic response. *Proc. Natl. Acad. Sci. USA* **105**, 19312–19317 (2008).
21. H. Laeverenz-Schlogelhofer, K. Y. Wan, Bioelectric control of locomotor gaits in the walking ciliate *Euplotes*. *Curr. Biol.* **34**, 697–709 (2024).
22. I. Elices, *et al.*, An electrophysiological and kinematic model of *Paramecium*, the "swimming neuron." *PLoS Comput. Biol.* **19**, e1010899 (2023).
23. H. de Maleprade, F. Moisy, T. Ishikawa, R. E. Goldstein, Motility and phototaxis of *Gonium*, the simplest differentiated colonial alga. *Phys. Rev. E.* **101**, 022416 (2020).
24. J. Manabe, T. Omori, T. Ishikawa, Shape matters: entrapment of a model ciliate at interfaces. *J. Fluid Mech.* **892**, A15 (2020).
25. C. J. Olson Reichhardt, C. Reichhardt, Ratchet effects in active matter systems. *Annu. Rev. Condens. Matter Phys.* **8**, 51–75 (2017).
26. T. Ohmura, *et al.*, Simple mechanosense and response of cilia motion reveal the intrinsic habits of ciliates. *Proc. Natl. Acad. Sci. USA* **115**, 3231–3236 (2018).

27. T. Ishikawa, K. Kikuchi, Biomechanics of *Tetrahymena* escaping from a dead end. *Proc. R. Soc. B.* **285**, 20172368 (2018).

28. T. Ohmura, *et al.*, Near-wall rheotaxis of the ciliate *Tetrahymena* induced by the kinesthetic sensing of cilia. *Sci. Adv.* **7**, eabi5878 (2021).

29. T. Ostapenko, *et al.*, Curvature-guided motility of microalgae in geometric confinement. *Phys. Rev. Lett.* **120**, 068002 (2018).

30. J. Cammann, *et al.*, Emergent probability fluxes in confined microbial navigation. *Proc. Natl. Acad. Sci. USA* **118**, e2024752118 (2021).

31. A. Théry, *et al.*, Rebound and scattering of motile: *Chlamydomonas* algae in confined chambers. *Soft Matter* **17**, 4857–4873 (2021).

32. S. Echigoya, K. Sato, O. Kishida, T. Nakagaki, Y. Nishigami, Switching of behavioral modes and their modulation by a geometrical cue in the ciliate *Stentor coeruleus*. *Front. Cell Dev. Biol.* **10**, 1021469 (2022).

33. N. Escoubet, R. Brette, L.-L. Pontani, A. M. Prevost, Interaction of the mechanosensitive microswimmer *Paramecium* with obstacles. *R. Soc. Open Sci.* **10**, 221645 (2023).

34. R. Di Leonardo, *et al.*, Boundary shape engineering for the spatial control of confined active particles. *arXiv* (2024).

35. V. Tartar, *The Biology of Stentor* (Pergammon Press, 1961).

36. P.-S. Song, Photosensory transduction in *Stentor coeruleus* and related organisms. *Biochim. Biophys. Acta, Rev. Bioenerg.* **639**, 1–29 (1981).

37. D. C. Wood, Parametric studies of the response decrement produced by mechanical stimuli in the protozoan, *Stentor coeruleus*. *J. Neurobiol.* **1**, 345–360 (1969).

38. D. Rajan, *et al.*, Single-cell analysis of habituation in *Stentor coeruleus*. *Curr. Biol.* **33**, 241–251 (2023).

39. L. Eckert, *et al.*, Biochemically plausible models of habituation for single-cell learning. *Curr. Biol.* **34**, 5646–5658 (2024).

40. H. S. Jennings, Studies on reactions to stimuli in unicellular organisms. IX.—on the behavior of fixed infusoria (Stentor and Vorticella), with special reference to the modifiability of protozoan reactions. *Am. J. Physiol.* **8**, 23–60 (1902).

41. J. P. Dexter, S. Prabakaran, J. Gunawardena, A complex hierarchy of avoidance behaviors in a single-cell eukaryote. *Curr. Biol.* **29**, 4323–4329 (2019).

42. M. K. Trinh, M. T. Wayland, S. Prabakaran, Behavioural analysis of single-cell aneural ciliate, *Stentor roeseli*, using machine learning approaches. *J. R. Soc. Interface* **16**, 20190410 (2019).

43. S. Shekhar, *et al.*, Cooperative hydrodynamics accompany multicellular-like colonial organization in the unicellular ciliate *Stentor*. *Nat. Phys.* **21** (2025).

44. K. Y. Wan, *et al.*, Reorganization of complex ciliary flows around regenerating *Stentor coeruleus*. *Phil. Trans. R. Soc. B* **375**, 20190167 (2020).

45. E. A. Andrews, Stentor's anchoring organs. *J. Morphol.* **77**, 219–232 (1945).

46. E. M. Ettienne, Control of contractility in *Spirostomum* by dissociated calcium ions. *J. Gen. Physiol.* **56**, 168–179 (1970).

47. H. Ishida, Y. Shigenaka, Cell model contraction in the ciliate *Spirostomum*. *Cell Motil. Cytoskeleton* **9**, 278–282 (1988).

48. T. Matsuoka, *et al.*, Cell models of *Blepharisma*: Ca^{2+}-dependent modification of ciliary movement and cell elongation. *Eur. J. Protistol.* **27**, 371–374 (1991).

49. C. Kung, Y. Saimi, Ca^{2+} channels of *Paramecium*: a multidisciplinary study. *Curr. Top. Membr. Transp.* **23**, 45–66 (1985).

50. R. Brette, Integrative neuroscience of *Paramecium*, a "swimming neuron." *eNeuro* **8**, 1–21 (2021).

51. Y. Naitoh, R. Eckert, Ionic mechanisms controlling behavioral responses of *Paramecium* to mechanical stimulation. *Science* **164**, 963–965 (1969).

52. I. Kunita, S. Kuroda, K. Ohki, T. Nakagaki, Attempts to retreat from a dead-ended long capillary by backward swimming in *Paramecium*. *Front. Microbiol.* **5**, 270 (2014).

53. I. Kunita, *et al.*, A ciliate memorizes the geometry of a swimming arena. *J. R. Soc. Interface* **13**, 20160155 (2016).

54. V. Tartar, "Pattern and substance in *Stentor*" in *Cellular Mechanics in Differentiation and Growth*, D. Rudnick, Ed. (Princeton University Press, 1957), pp. 73–100.

55. I. Scharf, A. Farji-Brener, "Wall-following behavior: its ultimate and proximate explanations, prevalence, and implications" in *Advances in the Study of Behavior*, J. Podos, S. Healy, Eds. (Elsevier, 2024), pp. 1–49.

56. V. Rothschild, Non-random distribution of bull spermatozoa in a drop of sperm suspension. *Nature* **198**, 1221–1222 (1963).

57. J. Elgeti, G. Gompper, Microswimmers near surfaces. *Eur. Phys. J. Spec. Top.* **225**, 2333–2352 (2016).

58. K. Ishimoto, Guidance of microswimmers by wall and flow: thigmotaxis and rheotaxis of unsteady squirmers in two and three dimensions. *Phys. Rev. E.* **96**, 043103 (2017).

59. E. Newman, Contraction in *Stentor coeruleus*: a cinematic analysis. *Science* **177**, 447–449 (1972).

60. R. Nicola, Microhabitats of ciliates: specific adaptations to different substrates. *Limnol. Oceanogr.* **34**, 1089–1097 (1989).

61. G. Mori, M. Mattioli, P. Madoni, N. Ricci, The ciliate communities of different habitats of lake massaciuccoli (Tuscany): species composition and distribution. *Ital. J. Zool.* **65**, 191–202 (1998).

62. T. M. Fenchel, *Ecology of Protozoa: The Biology of Free-Living Phagotrophic Protists* (Springer, 1987).

63. N. de Terra, Culture of *Stentor coeruleus* on *Colpidium campylum*. *J. Protozool.* **13**, 491–492 (1966).

64. J. Schindelin, *et al.*, Fiji: an open-source platform for biological-image analysis. *Nat. Methods* **9**, 676–682 (2012).

65. W. Foissner, S. Wölfl, Revision of the genus *Stentor* Oken (Protozoa, Ciliophora) and description of *S.araucanus* nov. spec, from South American lakes. *J. Plankton Res.* **16**, 255–289 (1994).

Acknowledgments
We would like to thank Takuji Ishikawa and Kenta Ishimoto for their useful discussions and comments on the theoretical aspects. We also thank Osamu Kishida and Norihiko Kamaya for collecting samples and discussing the ecological aspects. Taku Morimoto and the Division of Technical Staffs in the Research Institute for Electronic Science at Hokkaido University supported the fabrication technique.

Funding: This study was supported by the Sasakawa Scientific Research Grant from The Japan Science Society Grant No. 2021-6029 (SE), the Promotion Project for Young Investigators in Hokkaido University (TN, YN), the establishment of university fellowships towards the creation of science technology innovation Grant Number JPMJFS2101 (SE), the Sumitomo Foundation Fiscal 2023 Grant for Basic Science Research Projects 2300464 (SE), JSPS KAKENHI Grant Numbers JP21H05303 (TN), JP21H05308 (YN), JP21H05310 (TN, KS), JP23H04300 (KS), JP24K09388 (YN), JP24K23220 (SE) and JP25K17535 (TO).

Author contributions
Conceptualization: SE, KS, TN, YN; Methodology: SE, TN, YN; Software: TO; Formal Analysis: SE; Investigation: SE, TO; Resources: SE, TO, YN; Data Curation: SE, TO; Writing – Original Draft: SE; Writing – Review & Editing: SE, TO, KS, TN, YN; Visualization: SE, TO; Supervision: TN, YN; Funding Acquisition: SE, TO, KS, TN, YN

Competing interests: The authors declare no competing interests.

Data and materials availability: All data needed to evaluate the conclusions in the paper are present in the paper and/or the Supporting Information.

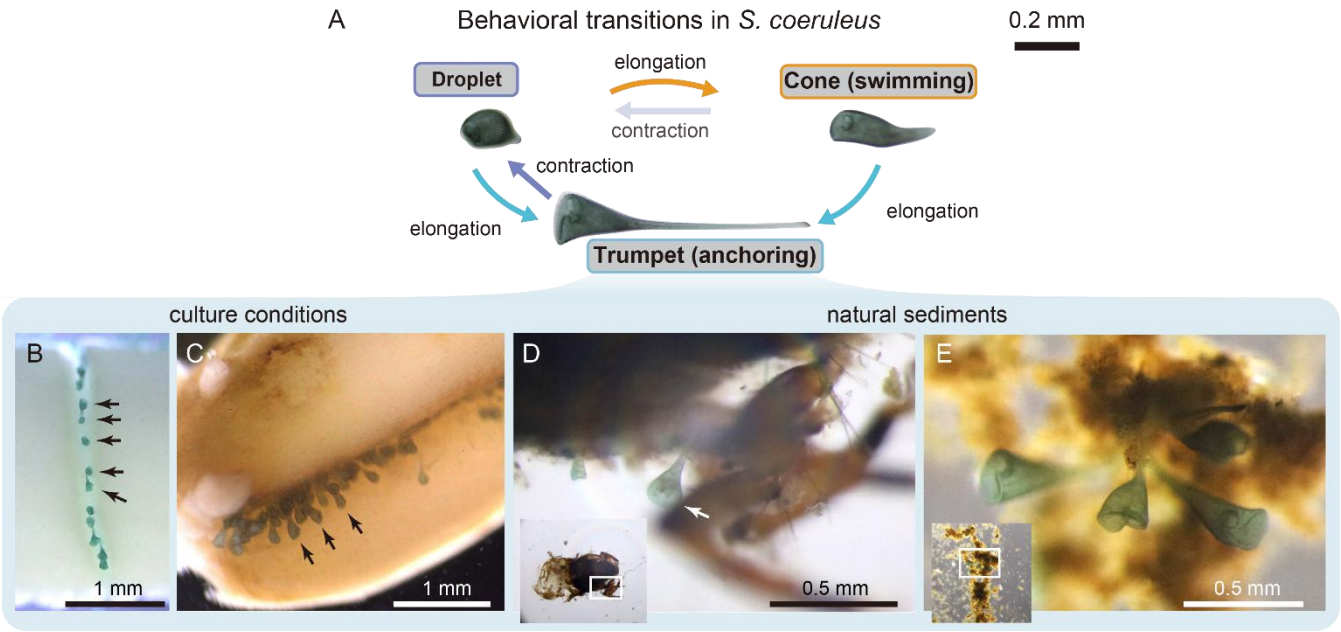

Fig. 1. Anchoring sites of *Stentor coeruleus* in natural and laboratory conditions.

(A) Three types of behavioral modes accompanying shape change in the ciliate *S. coeruleus*. Modified from Echigoya et al (32).
(B, C) Anchoring sites in culture conditions, such as the channel on a rice grain (B) and an oat grain (C). Each arrow indicates one anchoring *S. coeruleus*.
(D, E) Anchoring sites in natural sediments. *S. coeruleus* anchored to a narrow area in the larval exuvia of a caddisfly (Trichoptera) under laboratory conditions (D). Trumpet-shaped anchoring *S. coeruleus* were frequently observed on complex sediments upon sample collection from natural environment (E). The rectangles in the insets represent the focused regions.

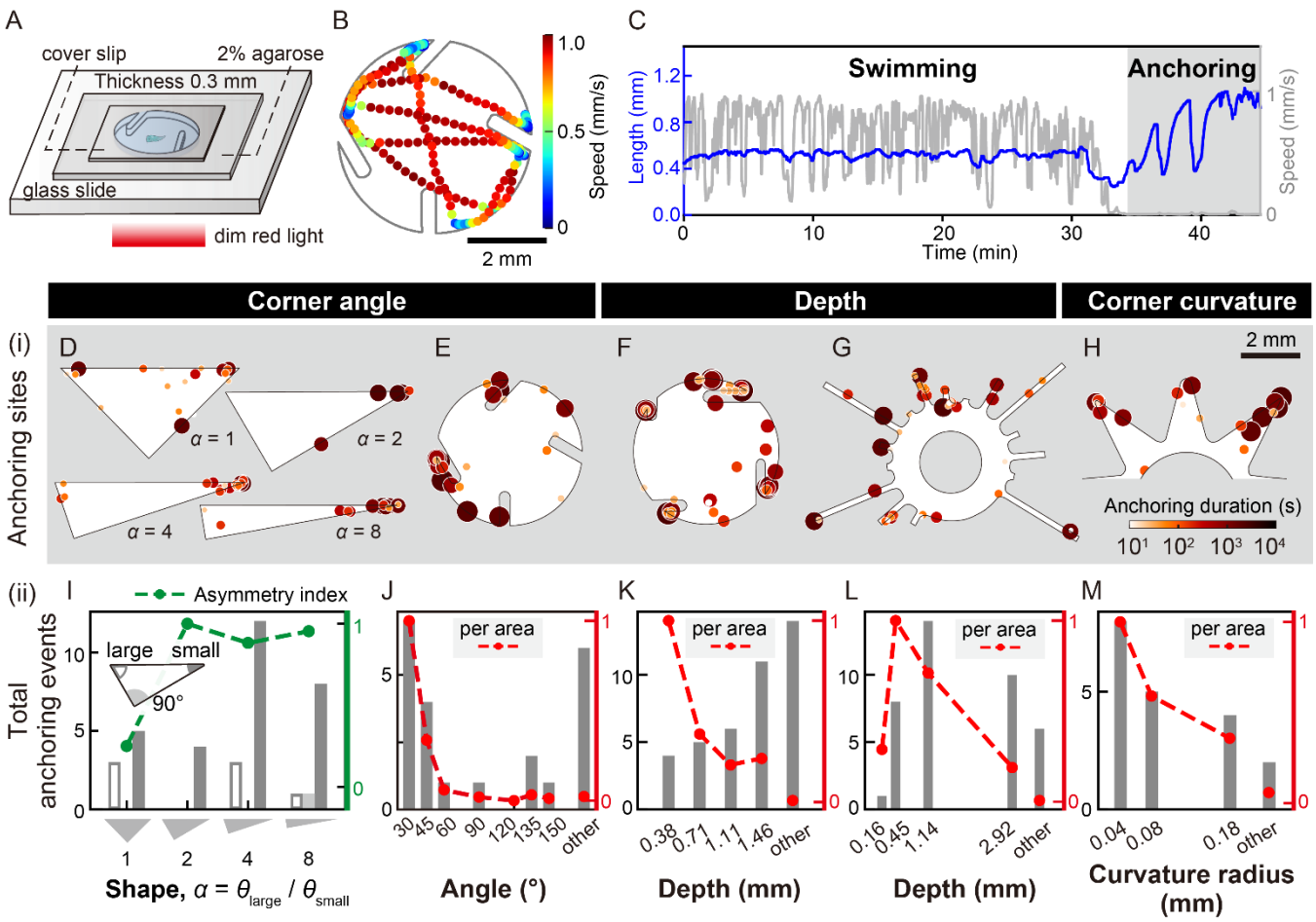

Fig. 2. Geometrical preferences of anchoring sites in geometrically complex environments in *Stentor coeruleus*.

(A) Experimental setup for behavioral observation in geometrical structural chambers. The behavior of *S. coeruleus* was observed in the chamber with a microstructure made of agarose gel and sealed with coverslip. Observation were conducted under weak red light to avoid phototactic responses in *S. coeruleus*.
(B) Swimming trajectory of *S. coeruleus* in a steady state in a geometrically structured chamber. Cell positions recorded every 0.25 s are plotted as points. Colors represent swimming speed.
(C) Overview of the behaviors focusing on the time series for swimming speed (gray line) and cell length (blue line), respectively. Swimming speed gradually decreased to zero as the cell transitioned from swimming to anchoring. This behavioral change was accompanied by a gradual elongation of the cell.
(D–H) Anchoring sites in several geometrically structured chambers. Each dot corresponds to an anchoring site. The color and size of the dots represent the duration of an anchoring event.
(I–M) Quantitative analysis of anchoring events in each specific area with different geometrical features within a chamber type. The green dashed line represents the asymmetry index calculated from the number of anchoring events divided by anchoring area (**i**). Red dashed lines are the anchoring frequencies, which were calculated as the number of anchoring events divided by anchoring area, normalized to a maximum value (J–M). The definitions of specific areas are included in Supplementary material, Fig. S1A–E. n = 7–9 cells in each chamber (D), n = 12 cells (E), n = 20 cells (F), n = 18 cells (G), and n = 15 cells (H). See also Supplementary material, Figs. S1–S3 and Movie S1.

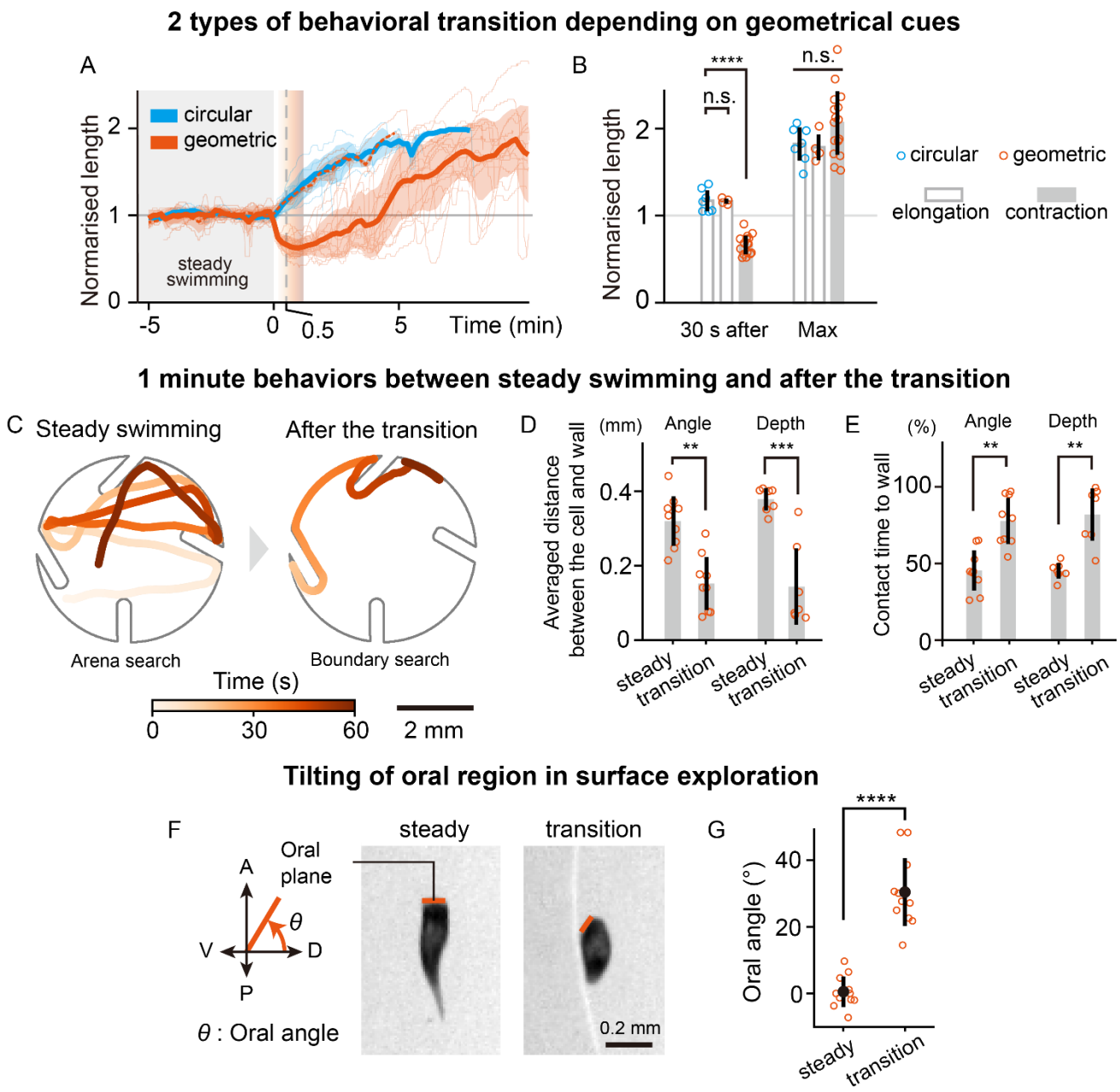

Fig. 3. Behavioral process of anchoring influenced by asymmetric deformation of body shape in geometrically structured chambers.

(A) Time series of cellular length in two behavioral transitions in the chamber with/without a geometrical structure. Cellular lengths were standardized by each individual mean pre-transition length, with the onset of transition aligned to $t = 0$. The thick solid lines and the thin colored areas correspond to the mean length and the standard deviation (SD) of the length, respectively. $n = 16$, contraction in the geometrically structured chambers; $n = 4$, elongation in the geometrically structured chambers; and $n = 7$ elongation in the simple circular chamber.

(B) Comparison of the normalized lengths in two transition types between the simple circular and geometrically structured chambers. The lengths 30 s after the transition were significantly different between the two behavioral processes (Welch's *t*-test; $p < 10^{-5}$; $t = 8.97$; one side; $n = 7$; $n = 16$). The lengths 30 s after the monotonic elongation process were not significantly different between the simple circular and geometrically structured chambers (Welch's *t*-test; $p = 0.93$; $t = 0.095$; $n = 7$; $n = 4$). There was no significant difference in the maximum normalized cell lengths after the transition (one-way ANOVA; $p = 0.15$; $F(2, 24) = 2.05$).

(C) Typical swimming trajectories over 1 min before and after the transition in the geometrically structured chamber. Color intensity represents time progression. Cells transitioned from broad exploration to surface exploration behavior.
(D) Quantification of surface exploration calculated as the mean distance between the wall and cell center in two geometrically structured chambers (paired *t*-test, angle; $p = 0.0024$, $t = -3.87$, one side, $n = 9$ cells; depth, $p = 0.00068$, $t = -5.62$, one side, $n = 7$ cells).
(E) Quantification of surface exploration calculated as the averaged ratio of wall-contact time to total time during the behavioral window of up to 1 minute (paired *t*-test, angle chamber; $p = 0.0044$, $t = 3.45$, one-side, 9 cells; depth chamber, $p = 0.0014$, $t = 4.87$, one side, $n = 7$ cells).
(F, G) Measurement of the oral plane of the cell. The tilted oral angle is defined as the angle between the anterior vector and the adjusted vector of the oral plane. The dorsal-to-anterior direction is a positive angle (F). Statistical analysis showed a significant difference in the tilted angle between the steady state and the transition state (G) (paired *t*-test, $p < 10^{-5}$, $t = -8.61$, $n = 11$ cells).
All error bars represent SDs. See also Supplementary material, Fig S4, Movie S2 and S3.

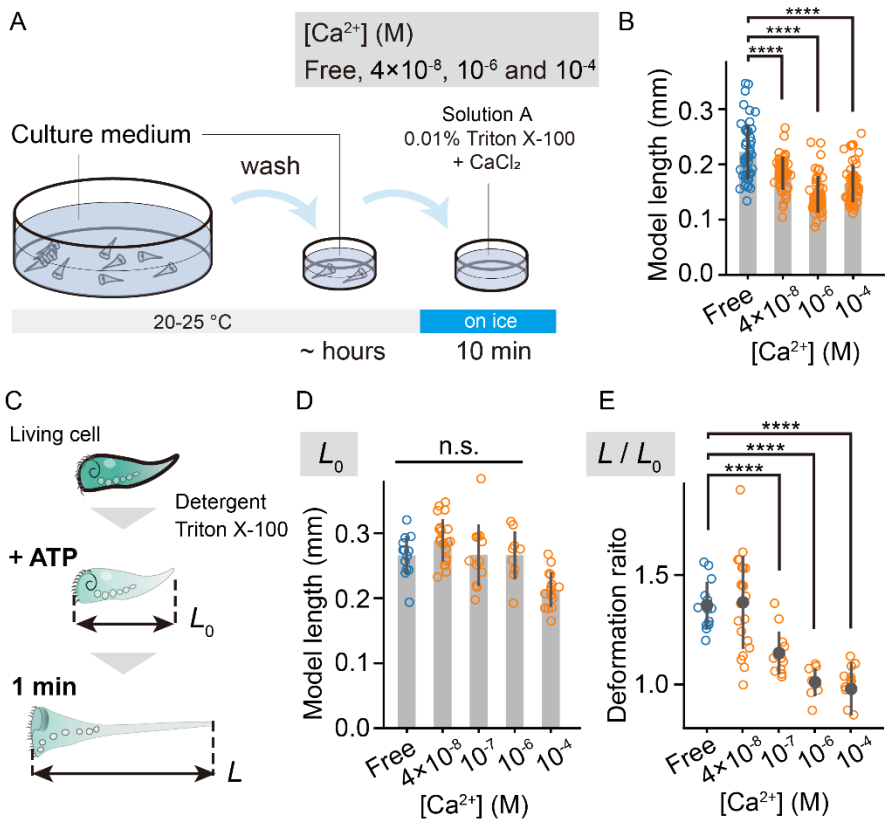

Fig. 4. Effects of Ca^{2+} concentration on the deformations of the Triton-extracted *Stentor coeruleus* model.

(A) Schematic diagram of the membrane extraction process at different Ca^{2+} concentrations.
(B) High Ca^{2+} concentrations promoted contraction of the model (Welch's *t*-test, $p < 10^{-5}$, $t = 4.62$ in 4×10^{-8} M; $p < 10^{-13}$, $t = 8.95$ in 10^{-6} M; $p < 10^{-8}$, $t = 6.68$ in 10^{-4} M, one side, $n = 47–51$).
(C) Schematics of the detergent-extracted model used to evaluate the effect of different Ca^{2+} concentrations on model elongation.
(D) Initial model lengths L_0 showed no significant difference at Ca^{2+} concentrations below 10^{-6} M (one-way ANOVA, $F(3, 51) = 1.58$, $p = 0.21$). The model length significantly decreased at high Ca^{2+} concentrations (10^{-4} M).
(E) Deformation ratio L / L_0 1 min after ATP addition at different Ca^{2+} concentrations (final concentration ~ 4 mM). For Ca^{2+} concentrations above 10^{-7} M, the elongation of the model was gradually suppressed (Welch's *t*-test, $p < 10^{-4}$, $t = 5.11$ in 10^{-7} M, $p < 10^{-8}$, $t = 9.23$ in 10^{-6} M, and $p < 10^{-8}$, $t = 8.54$ in 10^{-4} M, one side, $n = 9–21$).
All error bars represent SDs. See also Supplementary material, Fig. S5.

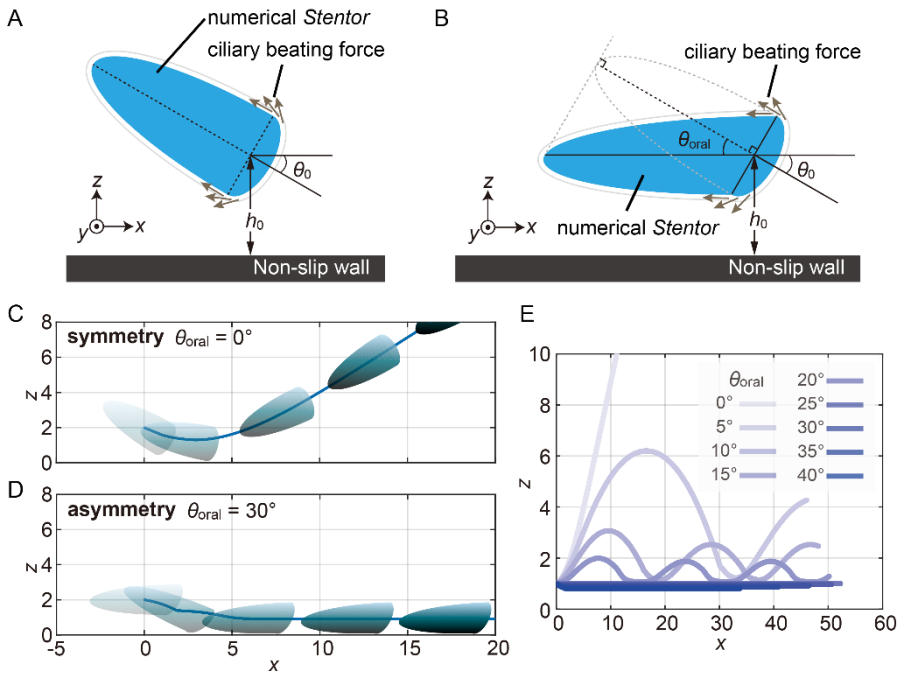

Fig. 5. Asymmetric propulsion of a conical swimmer physically explaining the wall-following swimming behavior.

(A) Schematic of the numerical simulation. A conical object, representing a simplified *Stentor* cell shape, deformed from a sphere of radius 1. The object at $(x, y, z) = (0, 0, 2)$ in the initial state faces the boundary wall at $z = 0$. Point forces, which correspond to the thrust forces from the beating MBs, are distributed peripherally around the base of the conical object tangency, directing the base to the vertex. **(B)** Schematic of the deformed swimmer. The elongated half of the swimmer horizontally shifts along the contracted hemisphere surface of the conical object (A). The initial condition and distribution in force are the same as (A).
(C, D) Time evolution and trajectories of symmetrical and asymmetrical swimmers. Each center of the swimmer is initially located at (0, 0, 2), and the locations of the conical swimmer are shown at 1, 200, 800, 1400, and 2000 numerical time steps. Although the symmetrical conical swimmer reflects the boundary owing to hydrodynamic interactions (C), the asymmetrical conical swimmer moves along the wall (D).
(E) Trajectories of the swimmer depending on the asymmetricity of the oral angle. Each center of the swimmer is initially located at (0, 0, 1), and the posterior axis horizontally aligns with the wall. See also Supplementary material, Fig. S6 and Movie S4.

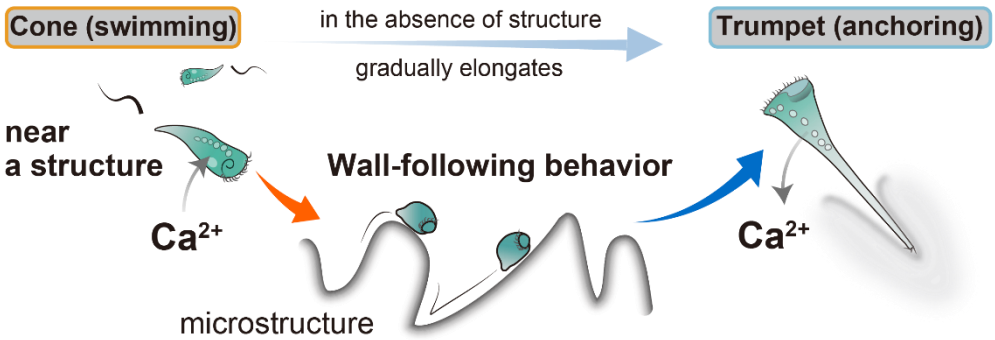

Fig. 6. Schematic illustration of the anchoring behavior in the presence of structures around the cell.

S. coeruleus usually swims with a helical trajectory during the steady swimming state. In the presence of nearby structures, frequent contact with the wall causes Ca^{2+} influx, triggering gradual cell contraction, and the cell exhibits an asymmetric propulsive force, physically inducing a wall-following behavior. Finally, the movement is physically regulated by the surrounding geometrical structures, and the deceleration facilitates anchoring. During the elongation process, Ca^{2+} efflux occurs. In contrast, in the absence of a structure, the cell gradually elongates from a conical swimming shape to a trumpet shape without contraction.